Influence functions for a hysteretic deformable mirror with a high-density 2D array of actuators

Schmerbauch, A. E. M.; Vasquez-Beltran, M. A.; Vakis, A.; Huisman, R.; Jayawardhana, B.

Published in:
Applied Optics

DOI:
10.1364/AO.397472

Research Article Vol. 59, No. 27 / 20 September 2020 / Applied Optics 8077

applied optics

Influence functions for a hysteretic deformable mirror with a high-density 2D array of actuators

A. E. M. Schmerbauch,[1,*] M. A. Vasquez-Beltran,[1] A. I. Vakis,[2] R. Huisman,[3] and B. Jayawardhana[1]

[1]Engineering and Technology Institute Groningen–Discrete Technology & Production Automation, Faculty of Science and Engineering, University of Groningen, 9747AG Groningen, The Netherlands
[2]Engineering and Technology Institute Groningen–Computational Mechanical and Materials Engineering, Faculty of Science and Engineering, University of Groningen, 9747AG Groningen, The Netherlands
[3]Netherlands Institute for Space Research, Groningen, The Netherlands
*Corresponding author: a.e.m.schmerbauch@rug.nl

Received 12 May 2020; revised 21 July 2020; accepted 3 August 2020; posted 4 August 2020 (Doc. ID 397472); published 11 September 2020

We present modeling and analysis of a hysteretic deformable mirror where the facesheet interacts with a continuous layer of piezoelectric material that can be actuated distributively by a matrix of electrodes through multiplexing. Moreover, a method to calculate the actuator influence functions is described considering the particular arrangement of electrodes. The results are presented in a semi-analytical model to describe the facesheet's deformation caused by a high-density array of actuators, and validated in a simulation. The proposed modeling of an interconnection layout of electrodes is used to determine the optimal pressures the actuators must exert to achieve a desired surface deformation.

https://doi.org/10.1364/AO.397472

1. INTRODUCTION

Deformable mirrors (DMs) are instruments used for the correction of light wavefront aberrations in many imaging and nonimaging applications such as three-dimensional (3D) imaging to increase the realism of depth perception [1,2], microscopes to correct static lenses [3], medical applications [4], or industrial applications like laser material processes [5]. In general, DMs are distinguished in segmented and continuous facesheet mirrors, and can be further classified by means of their actuator type that is mounted below the reflective top layer to deform the mirror surface. Depending on the application, various actuator technologies are used, which include, for example, piezoelectric [6–8], electrostatic [9], thermal [10,11], magneto-restrictive, and shape memory alloy [12] and voice coil/reluctance actuators [13,14]. Furthermore, DMs are applied in adaptive optical systems and key instruments for space telescopes. When a distorted incoming wavefront arrives at the telescope, a wavefront sensor is used to measure the wavefront distortion and subsequently used to adjust the shape of DM to correct the distorted wavefront. Future large space telescopes like LUVOIR [15] use coronographic instruments for high-contrast imaging of exoplanets. Although thousands of exoplanets have been identified, the current state of technology limits our capability to measure and understand these exoplanets beyond their mass, radius, orbital period, and distance to the host star. To overcome these challenges and provide the required capabilities for a direct exoplanet imaging space mission, DMs strive among others after high actuator density, meaning that the number of actuators must be increased to the maximum that can still guarantee practical operability for wire bonding, harness and electronics. DMs usually have a number of actuators ranging from 100 to 6000, but rarely higher [14,16,17]. One of the major limitations of employing the mirrors with a large number of actuators on a space mission is the reliability of the associated cable harness and electronics. If every actuator must be driven continuously to hold a specific position, a dedicated channel consisting of a digital-to-analog converter and a high voltage amplifier is required per actuator, which results in bulky electronics.

The recently presented concept of a high pixel number deformable mirror using piezoelectric hysteresis for stable shape configurations [18], an abbreviated hysteretic deformable mirror (HDM), demonstrates what we believe to the best of our knowledge is a new DM concept whose actuation mechanism consists of multilayered piezoelectric actuators with high hysteresis. Figure 1 shows a schematic illustration of the HDM. The high hysteresis of the newly developed piezoelectric material guarantees a remnant deformation of the mirror surface after the input has been removed. This property enables the combination of a simple electrode layout to define actuators at the intersections and use multiplexing to address those intersections. The control of the remnant of a single actuator is presented in [19].

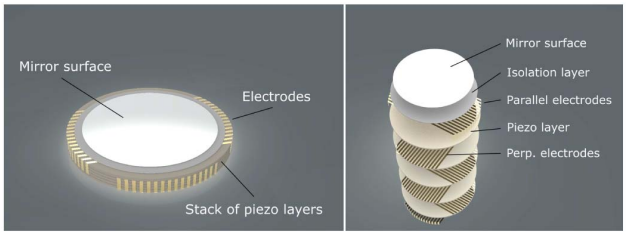

Fig. 1. 3D visualization of the mirror concept. The HDM consists of multilayered piezoelectric actuators that can deform the mirror surface by application of an electrical potential to the electrodes. Exploded view of the HDM with respective description of the individual components: mirror surface, isolation layer, parallel electrodes, piezo layers, and perpendicular electrodes.

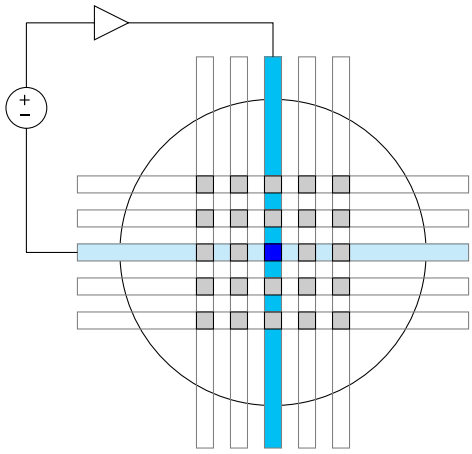

Fig. 2. Conceptual electrode layout of the hysteretic deformable mirror from the top view. As an example in the illustration, the central actuator is actuated by the application of an electrical potential to the center top and bottom electrodes, which are visualized in blue while the other (not activated) actuators are represented in gray.

The HDM focuses on applications where typically slowly varying disturbances (>1 Hz) must be corrected with extremely high accuracy ($<$ nm) and spatial frequency content, as it is the case for LUVOIR. Due to the HDM's design and working principle, it is possible to employ a large number of actuators (128×128) on an approximate surface area of 900 mm^2 and reach high-resolution accuracy in correcting wavefront aberrations. In addition, it benefits from time-division multiplexing, which reduces the number of wires needed to connect and address the actuators. Subsequently, the HDM provides a very simple electrode layout, as illustrated in Fig. 2. The top and bottom electrodes are rotated by 90° to form intersecting areas of the electrodes presenting the actuators. The actuation is bundled by sharing the same electrodes for actuators along a line. The voltage is transmitted over a shared top electrode while the corresponding bottom electrode for the desired actuator is grounded.

Motivated by what we believe is a novel concept, we present the modeling and analysis of a mirror's facesheet that is subjected to the key characteristics of the HDM, including a high actuator density and an interconnection layout. The mirror is described with a mechanical model to show the relation between the facesheet deflection and the pressures applied by the actuators. We follow the approach presented by Claflin and Bareket [20] in assuming that the deflection is governed by Poisson's equation. To guarantee a high accuracy in modeling, we incorporate the particular arrangement of the electrodes in the HDM into the solution of Poisson's equation and present the analytical solutions for the parametrization of squared electrodes as one of our contributions. In addition, an actuator model is introduced that incorporates the concept that the actuator's pressure is a function of hysteresis modeled by the Preisach operator. Based on this approach, we can compute the required pressures to fit several Zernike polynomials [21], which are the preferred representation for light wavefront aberrations in adaptive optical systems. The simulation is performed for low actuator numbers to demonstrate the calculation method with the given conditions, and high actuator numbers that will allow a high spatial frequency wavefront correction. The results, including the method's accuracy and limits of applicability, are discussed.

This paper has four sections. Section 2 presents the semi-analytical plate model to calculate the facesheet deflection caused by a high-density array with square pressure planes of the actuators interacting with the facesheet. Section 3 describes the least-square fitting to determine optimal actuator pressures to represent wavefront aberrations and presents simulation results for a 5×5 actuator array as well as a 129×129 actuator array. Finally, results are discussed and the conclusions are given in Section 4.

2. SEMI-ANALYTICAL PLATE MODEL

An influence function defines the characteristic shape of the mirror surface corresponding to the deformation caused by one actuator. Several methods currently exist for modeling these influence functions of continuous facesheet mirrors. Besides the use of Gauss functions and splines [22–24], or a biharmonic plate equation [25], influence functions can be modeled by application of the Kirchhoff or von Kármán theory [26–28] for plate deformations smaller than the plate thickness. Methods using the thin plate theory to calculate influence functions for real time computation for specific mirror geometries are given in [29,30]. Furthermore, models based on the Kirchhoff plate model, for example, include assumptions for actuator forces that either presuppose the exerted force as point load or approximated electrode areas with constantly distributed loads as well as boundary conditions presenting circularly clamped DMs [20,31] or a free outer edge [32]. Next to these modeling approaches which mainly consider the static characteristics, a detailed review and analysis of a DM's dynamic properties for control purposes can be found in [33].

To determine the influence functions as precisely as possible with static characteristics, it is necessary to define the interaction areas according to their actual shapes. Given the concept of the HDM, the electrodes have an interconnection layout that creates pressure planes lying under a thin circular facesheet. Since the upper electrodes are the closest layer to the facesheet besides the comparable thin isolation layer, which is neglected for simplicity of our modeling, we idealized these pressure planes as squares. The actuators are separated by a specified

distance. To describe the surface displacement, it is necessary to integrate over the area of each pressure plane. Therefore, each plane is separated into several areas that can be described by a coordinate transformation using Cartesian coordinates as well as the radial and angular limits. It is assumed that the thickness of electrodes can be neglected and the piezoelectric actuators modeled as springs in parallel to a force source over an area that creates pressure on the facesheet.

A. Determination of Influence Matrix

We consider the Poisson equation [34]

$$\nabla^2 z = -\frac{q}{T}, \tag{1}$$

which governs the relation between small surface displacements z of a thin facesheet with surface tension T generated by an exerted pressure q. The solution to Poisson's equation in polar coordinates (r, ϕ) can be given by

$$z(r, \phi, \bar{r}, \bar{\phi}) = C \iint_A \mathcal{F}(r, \phi, \bar{r}, \bar{\phi}(\bar{r}))q(\bar{r}, \bar{\phi})\mathrm{d}\bar{\phi}\mathrm{d}\bar{r}, \tag{2}$$

with

$$A = \{(\bar{r}, \bar{\phi})|\phi_1(\bar{r}) \le \bar{\phi} \le \phi_2(\bar{r}),\ 0 \le \bar{r} \le 1\}, \tag{3}$$

where $z(r, \phi)$ is the out-of-plane displacement of the thin facesheet, $(\bar{r}, \bar{\phi})$ are the integration variables, $q(\bar{r}, \bar{\phi})$ are the distributed forces over the particular electrode area, and constant $C = a^2/T$ contains the relation between the facesheet radius a and the surface tension for normalization of the function $\mathcal{F}$ to unity. The edge deflection and slopes are equal to zero. Furthermore, $\mathcal{F}$ is defined as

$$\mathcal{F}(r, \phi, \bar{r}, \bar{\phi}(\bar{r})) = \begin{cases} f_1(r, \phi, \bar{r}, \bar{\phi}(\bar{r})) \text{ if } & 0 < \bar{r} < r \\ f_2(r, \phi, \bar{r}, \bar{\phi}(\bar{r})) \text{ if } & r < \bar{r} < 1. \end{cases} \tag{4}$$

The resulting deflection will be the integral of $z(r, \phi, \bar{r}, \bar{\phi})$ over the area A of the facesheet

$$z(r, \phi) = \frac{q(r, \phi)a^2}{2\pi T} \int_0^1 \int_0^{2\pi} \mathcal{F}(r, \phi, \bar{r}, \bar{\phi}(\bar{r}))\mathrm{d}\bar{\phi}\mathrm{d}\bar{r}, \tag{5}$$

assuming that $q(\bar{r}, \bar{\phi})$ is a piecewise constant function on $R_1 < r < R_2$, which gives $q(r, \phi)$. Note that R_1 and R_2 designate the smallest and greatest radius to describe the electrodes, respectively.

Following the approach of Claflin and Bareket [20], the equation to calculate the surface deflection on a specific point on the clamped facesheet is

$$z(r, \phi) = \sum_{j=1}^{N_e} \mathcal{M}_{(r,\phi)j} q_{(r,\phi)j}, \tag{6}$$

where $\mathcal{M}$ represents the coefficients derived from the solutions of the Poisson equation, $q_{(r,\phi)j}$ are piecewise constant pressures exerted on the respective j-th electrode, and N_e is the total number of electrodes.

The exact shape of an electrode is defined via a coordinate transformation. It allows us to implement the information later to the Poisson's equation [Eq. (2)] and find a solution. The electrode is split into parts based on areas of radial limits. These radial limits are used to implement the transformation from Cartesian to polar coordinates. Thus, ϕ depends on r. For convenience, the integration with respect to ϕ is performed first, and results in

$$\begin{aligned} z(r, \phi) = \frac{q(r, \phi)}{2\pi} C\{&- \ln(r) \int_0^r \bar{r}(\phi_2(\bar{r}) - \phi_1(\bar{r})) \\ &- \bar{r} \sum_{n=1}^{\infty} \frac{1}{n^2} \left((\bar{r}r)^n - \left(\frac{\bar{r}}{r}\right)^n \right) \\ &\times [\sin(n(\phi_2(\bar{r}) - \phi)) - \sin(n(\phi_1(\bar{r}) - \phi))]\mathrm{d}\bar{r} \\ &+ \int_r^1 \bar{r} \ln\left(\frac{1}{\bar{r}}\right) (\phi_2(\bar{r}) - \phi_1(\bar{r})) \\ &- \bar{r} \sum_{n=1}^{\infty} \frac{1}{n^2} \left((\bar{r}r)^n - \left(\frac{r}{\bar{r}}\right)^n \right) \\ &\times [\sin(n(\phi_2(\bar{r}) - \phi)) - \sin(n(\phi_1(\bar{r}) - \phi))]\mathrm{d}\bar{r}\}. \end{aligned} \tag{7}$$

The introduced coordinate transformation is inserted and the integration with respect to r is solved as a function of the position of the electrodes. We define five cases according to the actuator position (Fig. 3): *Case 1*, central actuator; *Case 2*, diagonal actuators; *Case 3*, midline actuators; *Case 4*, actuators above the diagonals; and *Case 5*, actuators below the diagonal. The definition of each radial limit can be found in Table 1, and is visualized in Figs. 4–8 together with a respective pressure plane.

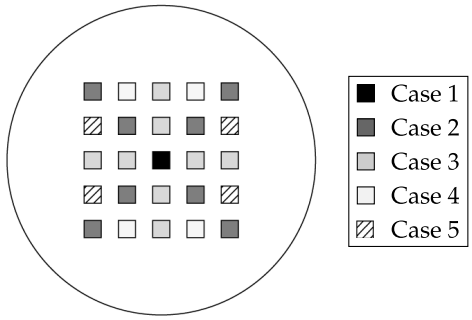

Fig. 3. Conceptual top view of a 5 × 5 actuator array to illustrate the classification of cases that arises from the geometric description and modeling method.

Table 1. Definition of Radial Limits for Splitting the Electrode Areas

Case 1	Case 2	Case 3	Case 4	Case 5
$\bar{r} = 0$	$\bar{r} \le r_1$	$\bar{r} \le r_{1e}$	$\bar{r} \le r_1$	$\bar{r} \le r_1$
$\bar{r} \ge r_1$	$\bar{r} \ge r_4$	$\bar{r} \ge r_4$	$\bar{r} \ge r_4$	$\bar{r} \ge r_4$
$0 < \bar{r} \le r_{1e}$	$r_1 < \bar{r} \le r_2$	$r_{1e} < \bar{r} \le r_1$	$r_1 < \bar{r} \le r_3$	$r_1 < \bar{r} \le r_2$
$r_{1e} < \bar{r} < r_1$	$r_2 < \bar{r} < r_4$	$r_1 < \bar{r} \le r_{4e}$	$r_3 < \bar{r} \le r_2$	$r_2 < \bar{r} \le r_3$
		$r_{4e} < \bar{r} < r_4$	$r_2 < \bar{r} < r_4$	$r_3 < \bar{r} < r_4$

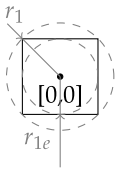

Fig. 4. Definitions of the radial limits to describe *Case 1*, central actuator.

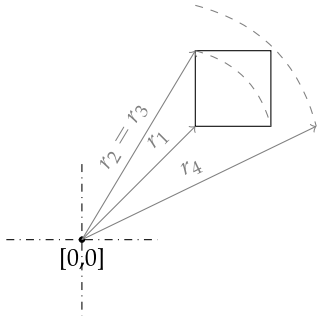

Fig. 5. Definitions of the radial limits to describe *Case 2*, diagonal actuator.

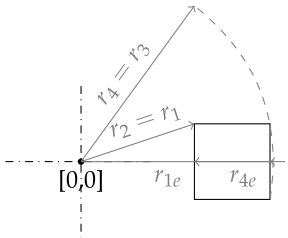

Fig. 6. Definitions of the radial limits to describe *Case 3*, midline actuator.

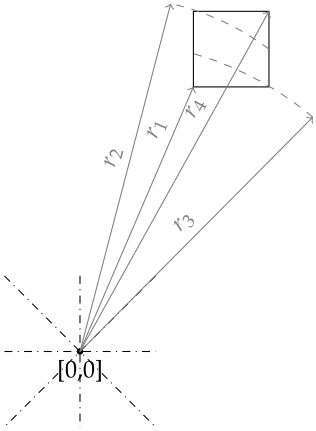

Fig. 7. Definitions of the radial limits to describe *Case 4*, actuators above the diagonal.

The detailed summary of the calculation of the coefficients resulting from the solution to Poisson's equation can be found in Appendices A–G.

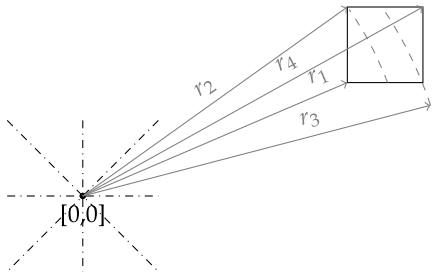

Fig. 8. Definitions of the radial limits to describe *Case 5*, actuators below the diagonal.

1. Case 1—Central Actuator

The central actuator (visualized in Fig. 4) was described by the use of two radial limits, r_1 and r_{1e}, where r_1 denotes the radius measured from the center to the corner points and r_{1e} denotes an extra radius measured from the center to the inner side length. The calculation of coefficients for this case can be found in Appendix C.

2. Case 2—Diagonal Actuators

The actuators that lie on the diagonals (visualized in Fig. 5) were described by the use of three radial limits: r_1, $r_2 = r_3$, and r_4. The numbering of the radii is systematically distributed according to the corner position. The calculation of coefficients for this case can be found in Appendix D.

3. Case 3–Midline Actuators

The actuators that lie on the midlines (visualized in Fig. 6) were described by use of four radial limits: r_{1e}, r_1, r_4, and r_{4e}. r_1 and r_4 denote radii measured from the center to certain corner points, and r_{1e} and r_{4e} denote extra radii indicating inner side lengths. The calculation of coefficients for this case can be found in Appendix E.

4. Case 4–Actuators Above the Diagonal

The actuators that lie above the diagonals (visualized in Fig. 7) were described by the use of four radial limits: r_1, r_3, r_2, and r_4. The numbering of the radii is systematically distributed according to the corner position. The calculation of coefficients for this case can be found in Appendix F.

5. Case 5—Actuators Below the Diagonal

The actuators that lie below the diagonals (visualized in Fig. 8) were described by the use of four radial limits: r_1, r_3, r_3, and r_4. The numbering of the radii is systematically distributed according to the corner position. The calculation of coefficients for this case can be found in Appendix G.

B. Actuator Model

The actuators become coupled through the stiffness of the facesheet. Usually, DMs profit by low inter-actuator coupling, denoting the mechanical coupling between neighboring

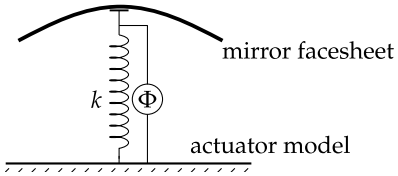

Fig. 9. Simplified actuator model, modeled by a stiffness k in parallel to a force source over an area Φ acting on the mirror facesheet.

actuators, which improves the surface accuracy. If significant inter-actuator coupling is present, it needs to be considered in the modeling and control processes [6]. Here, we introduce the model of actuators based on two components, which correspond to a spring in parallel with a force source (Fig. 9).

The pressure term $q(r, \phi)$ can be split so that it captures both components in terms of stiffness and force source over an area. Consequently, the relation from Eq. (6) may be described by

$$z(r, \phi) = \sum_{j=1}^{N_e} \mathcal{M}_{(r,\phi)j}(\Phi_{Pj}(V) - k_j \tilde{z_j}), \tag{8}$$

with

$$\Phi_{Pj}(V) = Y_j \Phi_{Tj}(V), \tag{9}$$

and

$$\tilde{z_j} := \frac{\sum_{i \in E_j} z_i / n_e}{A_e}, \tag{10}$$

where $\Phi_{Pj}(V)$ denotes the Preisach operator capturing the highly nonlinear hysteresis of the actuators in regard to the total deformation in relation to the initial thickness dimension, the diagonal matrix containing the Young's modulus Y_j, the longitudinal elongations of the actuators $\Phi_{Tj}(V)$, the diagonal stiffness matrix containing the actuators' stiffness k_j, and the mean surface deflection above the respective electrode with area A_e $\tilde{z}_j$ calculated by means of n_e surface displacement points z_i on a specific position within the electrode area. It is assumed that all the actuators are identical and can exert an asymmetric butterfly loop, as presented in Fig. 10. A framework to model the electric-field dependence on the strain in piezoelectric materials purposely designed to exhibit loops with remnant deformation was presented by Jayawardhana *et al.* [35] based on the use of the Preisach operator. The complete formal definition of the Preisach operator is given in [36].

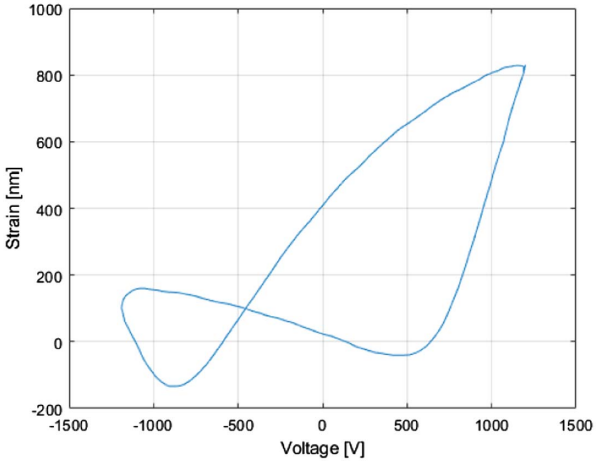

Fig. 10. Asymmetric butterfly hysteresis loop with remnant deformation, the measured data of which was collected from previous material tests. The axial displacement was measured while a certain voltage was applied.

3. RESULTS AND DISCUSSION

A. 2D Pattern for Influence Functions of Case 1–5

The influence function of every case can be seen in Fig. 11. The actuators were individually addressed, and their arrangement corresponds to the 5×5 actuator array that is exemplarily visualized in Fig. 3.

B. Least-Square Fitting

The preferred representation for light wavefront aberrations in adaptive optical systems is via Zernike polynomials. They are defined on a unit circle using polar coordinates (r, θ) as functions of azimuthal frequency m and radial degrees n, where $m \leq n$. The set of polynomials [21] can be given by

$$\begin{matrix} Z_n^m(r, \theta) = R_n^m(r) \cos(m\theta) & \text{for} & m \geq 0 \\ Z_n^{-m}(r, \theta) = R_n^m(r) \sin(m\theta) & \text{for} & m < 0 \end{matrix}, \tag{11}$$

where

$$R_n^m(r) = \sum_{S=0}^{(n-m)/2} \frac{(-1)^S (n-S)! r^{n-2S})}{S![(n+m)/2 - S]![(n-m)/2 - S!]}. \tag{12}$$

To calculate the required pressure terms to fit several Zernike polynomials, each displacement of a respective point on the facesheet that is defined by (r, ϕ) is fit to the corresponding point on Zernike polynomials. An overdetermined set of equations is solved in the least-square sense resulting in

$$\Phi = (\mathcal{M}^\intercal \mathcal{M})^{-1} \mathcal{M}(z_d + \mathcal{M} k \tilde{z}_d), \tag{13}$$

which aims to minimize the root-mean-square deviation (RMSD) between the two quantities.

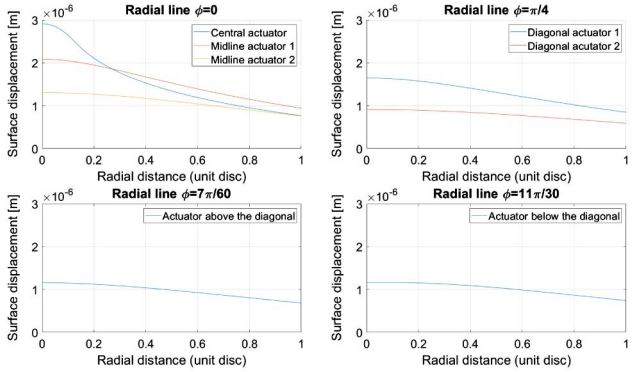

Fig. 11. Influence functions in the optically active area plotted along the radial line ϕ for *Case 1* and *Case 3* (top, left), *Case 2* (top, right), *Case 4* (bottom, left), and *Case 5* (bottom, right). Each actuator was addressed individually with a pressure of 0.01 Nm^{-2}.

C. Simulation Results

Using Matlab R2019a, a low-density array with 5 × 5 actuators and a high-density array with 129 × 129 actuators were generated. To decrease the computational effort in the latter case, the coefficient calculations were executed in parallel per five actuators and run in a compute cluster (Peregrine HPC cluster). For all experiments, we used a partition of two Intel Xeon E5 2680 v3 or v4 (2.50 GHz or 2.40 GHz, respectively) CPUs with 5 GB of memory. Thereby, the computational time was decreased to about 2 h when all jobs ran in parallel.

To assess the mechanical model, a second simulation in Matlab was generated fitting the mirror surface to selected Zernike polynomials. The procedure of this approach included three steps. The first step consisted of reducing the mirror surface to an optically active area due to the boundary conditions to circumvent an increasing fitting error caused by zero deflection at the clamped edge. Second, a mask was generated to match selected points of the Zernike polynomial disc plot to the surface points of the mirror. This mask was created with a partition in radial and angular coordinates according to $r_0 < r_1 < \ldots < r_{(n-1)} < r_n$ with $r_0 = 0$ and $r_n = 1$, and $\phi_0 < \phi_1 < \ldots < \phi_{(n-1)} < \phi_n$ with $\phi_0 = 0$ and $\phi_n = 2\pi$, respectively. In the third step, the RMSD of the estimator z_d with respect to the actual surface deflection z was calculated [Eq. (14)] to evaluate the mirror accuracy by

$$\mathrm{RMSD}(z) = \sqrt{\frac{\sum_{x=1}^{X} (z_x - z_{d_x})^2}{x}}. \tag{14}$$

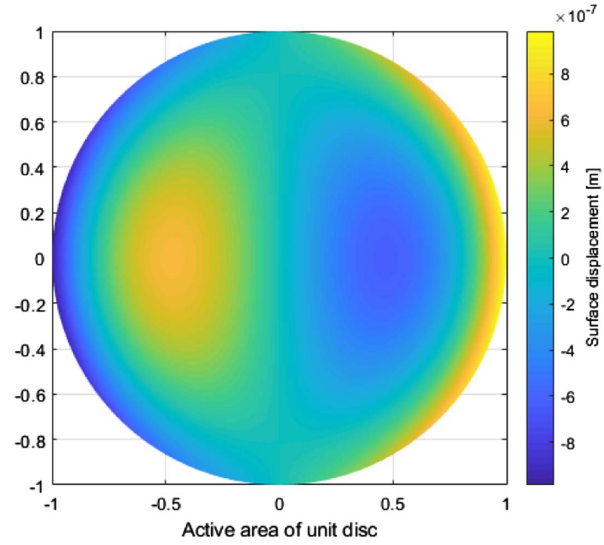

Fig. 12. 129 × 129 actuator array fitted to Zernike polynomial Z_3^1 with a peak-to-valley amplitude of 1.972 μm in a graphic representation showing the active area of the mirror as unit disc with a vertical colorbar giving the surface displacement.

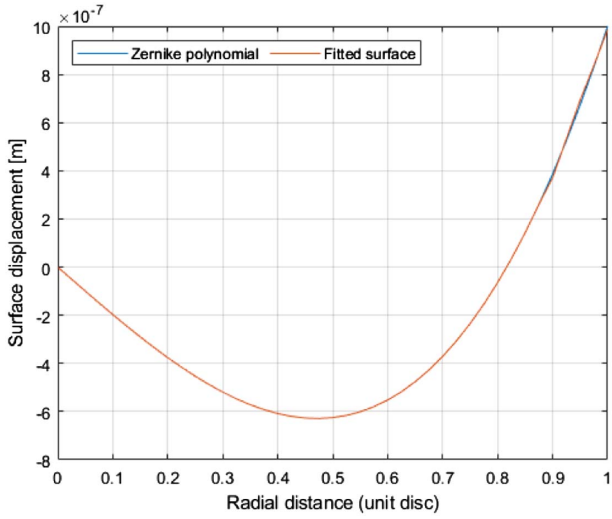

Fig. 13. Surface displacement along the radial line $\phi = 0$ for a 129 × 129 actuator array fitted to Zernike polynomial Z_3^1 with a peak-to-valley amplitude of 1.972 μm.

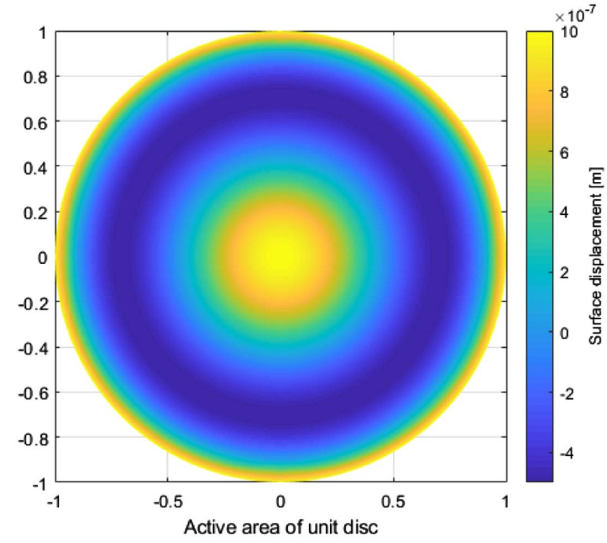

Fig. 14. 129 × 129 actuator array fitted to Zernike polynomial Z_4^0 with a peak-to-valley amplitude of 1.199 μm in a graphic representation showing the active area of the mirror as unit disc with a vertical colorbar giving the surface displacement.

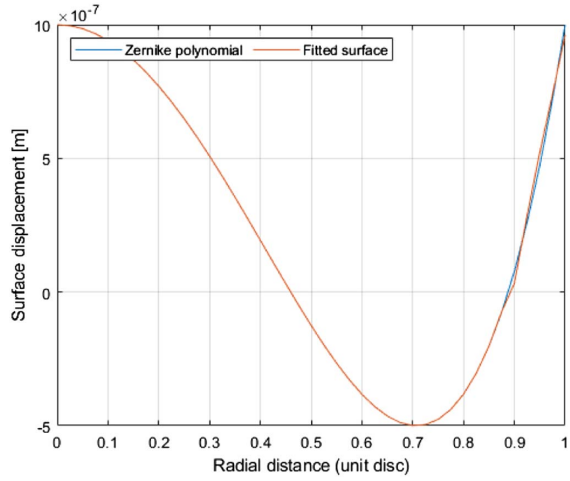

Fig. 15. Surface displacement along the radial line $\phi = 0$ for a 129 × 129 actuator array fitted to Zernike polynomial Z_4^0 with a peak-to-valley amplitude of 1.199 μm.

There were 4961 surface points selected based on the described partition over a diameter of 0.8, which corresponds to the active area. The facesheet surface tension amounted to 15 N m^{-2} and total mirror radius normalized to 1. Figures 12–15 show the results for a 129 × 129 actuator array of fitting the mirror surface to lower-order Zernike polynomials while Figs. 16 and 17 show the results for a selected higher-order polynomial. Table 2 summarizes the RMSDs for the first 28 Zernike polynomials and selected higher-order ones fitted with a peak-to-valley amplitude in the region of approximately 1.5 to 2 μm with a low- and high-density array.

Considering the fitting results for a low-density array with 5 × 5 actuators (25 actuators in the active area), the intersection layout became clear and the positions of the few actuators play a major role for the final results. The fitting errors are

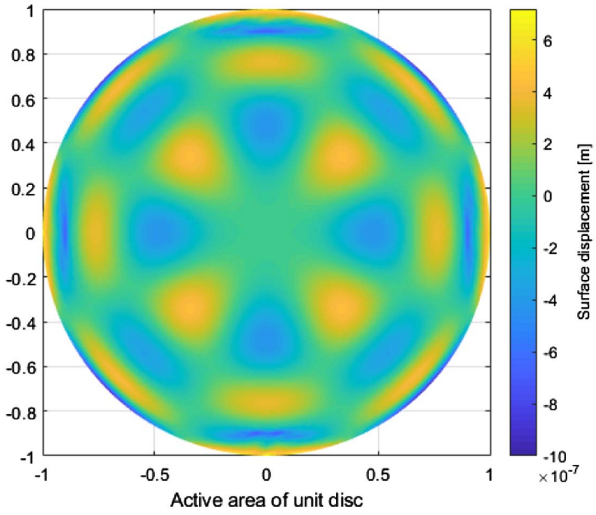

Fig. 16. 129 × 129 actuator array fitted to Zernike polynomial Z_{10}^{4} with a peak-to-valley amplitude of 1.718 μm in a graphic representation showing the active area of the mirror as unit disc with a vertical colorbar giving the surface displacement.

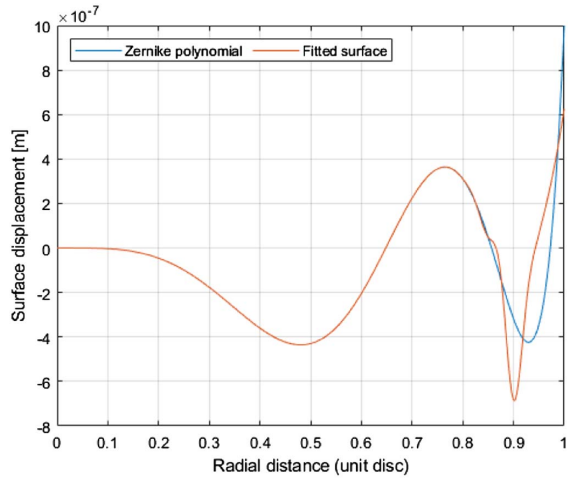

Fig. 17. Surface displacement along the radial line $\phi = 0$ for a 129 × 129 actuator array fitted to Zernike polynomial Z_{10}^{4} with a peak-to-valley amplitude of 1.718 μm.

Table 2. Summary of Root-Mean-Square Deviations (RMSDs) for Selected Zernike Polynomials (ZPs) with a 5 × 5 [Low Density (LD)] and 129 × 129 Actuator Array [High Density (HD)]

ZPs	LD: RMSDs in [%]	HD: RMSDs in [%]
Z_1^{-1}	4.426	0.001433
Z_1^{1}	4.352	0.001373
Z_2^{-2}	3.806	0.000298
Z_2^{0}	12.840	0.065971
Z_2^{2}	9.498	0.004775
Z_3^{-3}	10.138	0.007609
Z_3^{-1}	13.937	0.131942
Z_3^{1}	13.756	0.134622
Z_3^{3}	9.974	0.007343
Z_4^{-4}	11.376	0.005252
Z_4^{-2}	12.662	0.082268
Z_4^{0}	25.917	0.524411
Z_4^{2}	20.755	0.409452
Z_4^{4}	13.069	0.011954
Z_5^{-5}	13.847	0.017128
Z_5^{-3}	18.909	0.406282
Z_5^{-1}	18.838	0.675500
Z_5^{1}	18.674	0.692096
Z_5^{3}	18.717	0.400501
Z_5^{5}	13.649	0.016273
Z_6^{-6}	14.903	0.009467
Z_6^{-4}	20.851	0.364835
Z_6^{-2}	18.077	0.346565
Z_6^{0}	25.742	1.735849
Z_6^{2}	17.145	1.670824
Z_6^{4}	16.980	0.729995
Z_6^{6}	14.790	0.049802
Z_{10}^{-10}	16.216	0.087481
Z_{10}^{-8}	18.114	1.420633
Z_{10}^{-6}	18.901	2.341578
Z_{10}^{-4}	20.592	2.417903
Z_{10}^{-2}	22.680	1.451910
Z_{10}^{0}	27.243	6.092243
Z_{10}^{2}	21.649	6.225307
Z_{10}^{4}	18.076	4.505920
Z_{10}^{6}	18.868	3.345968
Z_{10}^{8}	17.221	1.468534
Z_{10}^{10}	17.303	0.271556

between 3.8% and 27.2%. Comparing these results to a high-density array with 129 × 129 actuators (16073 actuators in the active area, 568 actuators outside), we observe that the RMSDs decrease drastically. With 129 × 129 actuators, we have deviations between 0.000298% and 6.23% for the selected polynomials. For higher-order polynomials, corner effects are visible. Although the fitting errors for low- and high-density arrays behave in a similar manner with an increasing degree of the polynomial, it is noticeable that with Zernike polynomials in the cosine phase, the RMSD is slightly higher due to the square grid that characterizes the HDM. For further fitting improvement, the position of the square region, in which the actuators are created due to the interconnection of electrodes, might be adjusted with the active area to cover completely upper, lower, left, and right corners of the unit disc.

4. CONCLUSIONS

This study investigated the fundamental characteristics of actuator positions of high-density arrays and presented a generalization of cases to calculate every actuator position of deformable mirrors for application in what we believe to the best of our knowledge is a novel hysteretic deformable mirror. Based on the introduced coordinate transformation while solving the Poisson equation, it was possible to exactly model the shape of the pressure planes and guarantee a more realistic description of the actuator influence functions. By calculating the coefficient matrix in a cluster, the computational time was decreased, which presents a usable method for computations on deformable mirrors with high actuator densities. Furthermore, the mirror model includes the mechanical coupling between the actuators and the facesheet. The presented results contribute to achieve a higher accuracy in modeling the actuator influence functions according to the actual properties of the DM, and therefore decrease fitting errors. It provides a framework on how to consider high actuator densities and calculate them in a reasonable way regarding actuator position case classification and computation time.

APPENDIX A: RESPECTIVE FORMULAS

For actuators of the right side of the plate, the left corner of a pressure plane is denoted with x_1, the right corner with x_2, the lower corner with y_1, and the upper corner with y_2.

Table 3. Definition of Radial Limits in Interval *I* with Coordinate Transformation for Splitting the Electrode Areas

Case 1	Boundaries	Coordinate transformation
I_1	$0 \le \bar{r} \le r_{1e}$	$0 < \bar{\phi} < 2\pi$
I_{21}	$r_{1e} < \bar{r} < r_1$	$\arccos(x_2/\bar{r}) < \bar{\phi} < \arcsin(y_2/\bar{r})$
I_{22}		$\arcsin(y_2/\bar{r}) < \bar{\phi} < \arccos(x_1/\bar{r})$
I_{23}		$\arccos(x_1/\bar{r}) < \bar{\phi} < \arcsin(y_1/\bar{r})$
I_{24}		$\arcsin(y_1/\bar{r}) < \bar{\phi} < \arccos(x_2/\bar{r})$
Case 2	**Boundaries**	**Coordinate transformation**
I_1	$r_1 < \bar{r} \le r_2$	$\arcsin(y_1/\bar{r}) < \bar{\phi} \le \arccos(x_1/\bar{r})$
I_2	$r_2 < \bar{r} < r_4$	$\arccos(x_2/\bar{r}) < \bar{\phi} < \arcsin(y_2/\bar{r})$
Case 3	**Boundaries**	**Coordinate transformation**
I_{11}	$r_{1e} < \bar{r} \le r_1$	$0 < \bar{\phi} \le \arccos(x_1/\bar{r})$
I_{12}		$2\pi - \arccos(x_1/\bar{r}) < \bar{\phi} < 2\pi$
I_2	$r_1 < \bar{r} \le r_{4e}$	$\arcsin(y_1/\bar{r}) < \bar{\phi} \le \arcsin(y_2/\bar{r})$
I_{31}	$r_{4e} < \bar{r} < r_4$	$\arccos(x_2/\bar{r}) < \bar{\phi} < \arcsin(y_2/\bar{r})$
I_{32}		$\arcsin(y_1/\bar{r}) < \bar{\phi} < \arccos(x_2/\bar{r})$
Case 4	**Boundaries**	**Coordinate transformation**
I_1	$r_1 < \bar{r} \le r_3$	$\arcsin(y_1/\bar{r}) < \bar{\phi} \le \arccos(x_1/\bar{r})$
I_2	$r_3 < \bar{r} \le r_2$	$\arccos(x_2/\bar{r}) < \bar{\phi} \le \arccos(x_1/\bar{r})$
I_3	$r_2 < \bar{r} < r_4$	$\arccos(x_2/\bar{r}) < \bar{\phi} < \arcsin(y_2/\bar{r})$
Case 5	**Boundaries**	**Coordinate transformation**
I_1	$r_1 < \bar{r} \le r_2$	$\arcsin(y_1/\bar{r}) < \bar{\phi} \le \arccos(x_1/\bar{r})$
I_2	$r_2 < \bar{r} \le r_3$	$\arcsin(y_1/\bar{r}) < \bar{\phi} \le \arcsin(y_2/\bar{r})$
I_3	$r_3 < \bar{r} < r_4$	$\arccos(x_2/\bar{r}) < \bar{\phi} < \arcsin(y_2/\bar{r})$

Table 4. Assignment of Symbols to Reoccurring Formulas

Symbol	Formula	Symbol	Formula
κ_{x_1}	$x_1\sqrt{1-x_1^2/r^2}$	κ_{y_1}	$y_1\sqrt{1-y_1^2/r^2}$
κ_{x_2}	$x_2\sqrt{1-x_2^2/r^2}$	κ_{y_2}	$y_2\sqrt{1-y_2^2/r^2}$
ϵ_{x_1}	$x_1\sqrt{(r^2-x_1^2)/r^2}$	ϵ_{y_1}	$y_1\sqrt{(r^2-y_1^2)/r^2}$
ϵ_{x_2}	$x_2\sqrt{(r^2-x_2^2)/r^2}$	ϵ_{y_2}	$y_2\sqrt{(r^2-y_2^2)/r^2}$
α_1	$\arccos(x_1/r)$	α_2	$\arccos(x_2/r)$
β_1	$\arcsin(y_1/r)$	β_2	$\arcsin(y_2/r)$
γ_1	$\arcsin(x_1/r)$	γ_2	$\arcsin(x_2/r)$

The designation is mirrored with actuators on the left side of the plate. In general, it can be said that $|x_1| \le |x_2|$ and $|y_1| \le |y_2|$.

Table 3 summarizes the definition of all radial limits with coordinate transformations for splitting the electrode areas. The symbols assigned to reoccurring formulas are listed in Table 4.

APPENDIX B: NUMERICAL INTEGRATION

Here are the two subintegrals that are solved numerically. 174 is the maximum number of n terms required for convergence [20], so

$$f_{1n} := \sum_{n=1}^{\infty} \int_{R_1}^{R_2} \frac{\bar{r}}{n^2} \left((\bar{r}r)^n - \left(\frac{\bar{r}}{r}\right)^n \right) \times [\sin(n(\phi_2(\bar{r}) - \phi)) - \sin(n(\phi_1(\bar{r}) - \phi))] \mathrm{d}\bar{r}$$

$$f_{2n} := \sum_{n=1}^{\infty} \int_{R_1}^{R_2} \frac{\bar{r}}{n^2} \left((\bar{r}r)^n - \left(\frac{r}{\bar{r}}\right)^n \right) \times [\sin(n(\phi_2(\bar{r}) - \phi)) - \sin(n(\phi_1(\bar{r}) - \phi))] \mathrm{d}\bar{r}.$$

APPENDIX C: COEFFICIENT CALCULATION IN CASE 1

Here are the formulas to calculate the coefficients $\mathcal{M}$ for actuators that can be categorized in *Case 1*:

$$\begin{aligned} &r_i = 0 \\ &\mathcal{M} = (1/(2\pi)) \times ((f_{2(I_1)}(r_{1e})) + (f_{2(I_{21})}(r_1) - f_{2(I_{21})}(r_{1e})) \\ &\quad + (f_{2(I_{22})}(r_1) - f_{2(I_{22})}(r_{1e})) + (f_{2(I_{23})}(r_1) - f_{2(I_{23})}(r_{1e})) \\ &\quad + (f_{2(I_{24})}(r_1) - f_{2(I_{24})}(r_{1e}))), \end{aligned} \tag{C1}$$

$$\begin{aligned} &0 < r_i \le r_{1e}, \\ &\mathcal{M} = (1/(2\pi)) \times ((f_{1(I_1)}(r_i) - f_{1(I_1)}(0)) - f_{1n(I_1)} \\ &\quad + (f_{2(I_1)}(r_{1e}) - f_{2(I_1)}(r_i)) - f_{2n(I_1)} \\ &\quad + (f_{2(I_{21})}(r_1) - f_{2(I_{21})}(r_{1e})) - f_{2n(I_{21})} \\ &\quad + (f_{2(I_{22})}(r_1) - f_{2(I_{22})}(r_{1e})) - f_{2n(I_{22})} \\ &\quad + (f_{2(I_{23})}(r_1) - f_{2(I_{23})}(r_{1e})) - f_{2n(I_{23})} \\ &\quad + (f_{2(I_{24})}(r_1) - f_{2(I_{24})}(r_{1e})) - f_{2n(I_{24})}), \end{aligned} \tag{C2}$$

$$r_{1e} < r_i < r_1,$$

$$\begin{aligned}\mathcal{M} = (1/(2\pi)) \times ((&f_{1(I_{21})}(r_i) - f_{1(I_{21})}(r_{1e})) - f_{1n(I_{21})} \\ &+ (f_{1(I_{22})}(r_i) - f_{1(I_{22})}(r_{1e})) - f_{1n(I_{22})} \\ &+ (f_{1(I_{23})}(r_i) - f_{1(I_{23})}(r_{1e})) - f_{1n(I_{23})} \\ &+ (f_{1(I_{24})}(r_i) - f_{1(I_{24})}(r_{1e})) - f_{1n(I_{24})} \\ &+ (f_{2(I_{21})}(r_1) - f_{2(I_{21})}(r_i)) - f_{2n(I_{21})} \\ &+ (f_{2(I_{22})}(r_1) - f_{2(I_{22})}(r_i)) - f_{2n(I_{22})} \\ &+ (f_{2(I_{23})}(r_1) - f_{2(I_{23})}(r_i)) - f_{2n(I_{23})} \\ &+ (f_{2(I_{24})}(r_1) - f_{2(I_{24})}(r_i)) - f_{2n(I_{24})} \\ &+ (f_{1(I_1)}(r_{1e}) - f_{1(I_1)}(0)) - f_{1n(I_1)}),\end{aligned} \tag{C3}$$

$$r_i \geq r_1,$$

$$\begin{aligned}\mathcal{M} = (1/(2\pi)) \times ((&f_{1(I_1)}(r_{1e}) - f_{1(I_1)}(0)) - f_{1n(I_1)} \\ &+ (f_{1(I_{21})}(r_1) - f_{1(I_{21})}(r_{1e})) - f_{1n(I_{21})} \\ &+ (f_{1(I_{22})}(r_1) - f_{1(I_{22})}(r_{1e})) - f_{1n(I_{22})} \\ &+ (f_{1(I_{23})}(r_1) - f_{1(I_{23})}(r_{1e})) - f_{1n(I_{23})} \\ &+ (f_{1(I_{24})}(r_1) - f_{1(I_{24})}(r_{1e})) - f_{1n(I_{24})})\end{aligned} \tag{C4}$$

A. Sub-Functions of f_1

$$f_{1(I_1)} = -(\pi r^2 \log(r_i))$$

$$f_{1(I_{21})} = (r(-(\kappa_{x_2}) - \kappa_{y_2} + r\alpha_2 - r\beta_2)\log(r_i))/2$$

$$f_{1(I_{22})} = (r(\kappa_{x_1} + \kappa_{y_2} - r\alpha_1 + r\beta_2)\log(r_i))/2$$

$$f_{1(I_{23})} = (r(-(\kappa_{x_1}) - \kappa_{y_1} + r\alpha_1 - r\beta_1)\log(r_i))/2$$

$$f_{1(I_{24})} = (r(\kappa_{x_2} + \kappa_{y_1} - r\alpha_2 + r\beta_1)\log(r_i))/2$$

B. Sub-Functions of f_2

$$f_{2(I_1)} = 2\pi(r^2/4 + (r^2\log(r^{-1}))/2)$$

$$\begin{aligned}f_{2(I_{21})} = &(3r\epsilon_{x_2})/4 + (3r\epsilon_{y_2})/4 - (r^2\alpha_2)/4 + (x_2^2\gamma_2)/2 \\ &+ (r^2\beta_2)/4 + (y_2^2\beta_2)/2 + (r(\epsilon_{x_2} - r\alpha_2)\log(r^{-1}))/2 \\ &+ (r(\epsilon_{y_2} + r\beta_2)\log(r^{-1}))/2\end{aligned}$$

$$\begin{aligned}f_{2(I_{22})} = &(-3r\epsilon_{x_1})/4 - (3r\epsilon_{y_2})/4 + (r^2\alpha_1)/4 - (x_1^2\gamma_1)/2 \\ &- (r^2\beta_2)/4 - (y_2^2\beta_2)/2 - (r(\epsilon_{x_1} - r\alpha_1)\log(r^{-1}))/2 \\ &- (r(\epsilon_{y_2} + r\beta_2)\log(r^{-1}))/2\end{aligned}$$

$$\begin{aligned}f_{2(I_{23})} = &(3r\epsilon_{x_1})/4 + (3r\epsilon_{y_1})/4 - (r^2\alpha_1)/4 + (x_1^2\gamma_1)/2 \\ &+ (r^2\beta_1)/4 + (y_1^2\beta_1)/2 + (r(\epsilon_{x_1} - r\alpha_1)\log(r^{-1}))/2 \\ &+ (r(\epsilon_{y_1} + r\beta_1)\log(r^{-1}))/2\end{aligned}$$

$$\begin{aligned}f_{2(I_{24})} = &(-3r\epsilon_{x_2})/4 - (3r\epsilon_{y_1})/4 + (r^2\alpha_2)/4 - (x_2^2\gamma_2)/2 \\ &- (r^2\beta_1)/4 - (y_1^2\beta_1)/2 - (r(\epsilon_{x_2} - r\alpha_2)\log(r^{-1}))/2 \\ &- (r(\epsilon_{y_1} + r\beta_1)\log(r^{-1}))/2\end{aligned}$$

APPENDIX D: COEFFICIENT CALCULATION IN CASE 2

Here are the formulas to calculate the coefficients $\mathcal{M}$ for actuators that can be categorized in *Case 2*:

$$r_i \leq r_1,$$

$$\begin{aligned}\mathcal{M} = (1/(2\pi))(&(f_{2(I_1)}(r_2) - f_{2(I_1)}(r_1)) - f_{2n(I_1)}) \\ &+ ((f_{2(I_2)}(r_4) - f_{2(I_2)}(r_2)) - f_{2n(I_2)}))\end{aligned} \tag{D1}$$

$$r_1 < r_i \leq r_2,$$

$$\begin{aligned}\mathcal{M} = (1/(2\pi))(&(f_{1(I_1)}(r_i) - f_{1(I_1)}(r_1)) - f_{1n(I_1)}) \\ &+ ((f_{2(I_1)}(r_2) - f_{2(I_1)}(r_i)) - f_{2n(I_1)}) \\ &+ ((f_{2(I_2)}(r_4) - f_{2(I_2)}(r_2)) - f_{2n(I_2)}))\end{aligned} \tag{D2}$$

$$r_2 < r_i < r_4,$$

$$\begin{aligned}\mathcal{M} = (1/(2\pi))(&(f_{1(I_2)}(r_i) - f_{1(I_2)}(r_2)) - f_{1n(I_2)}) \\ &+ ((f_{2(I_2)}(r_4) - f_{2(I_2)}(r_i)) - f_{2n(I_2)}) \\ &+ ((f_{1(I_1)}(r_2) - f_{1(I_1)}(r_1)) - f_{1n(I_1)}))\end{aligned} \tag{D3}$$

$$r_i \geq r_4,$$

$$\begin{aligned}\mathcal{M} = (1/(2\pi))(&(f_{1(I_1)}(r_2) - f_{1(I_1)}(r_1)) - f_{1n(I_1)}) \\ &+ ((f_{1(I_2)}(r_4) - f_{1(I_2)}(r_2)) - f_{1n(I_2)}))\end{aligned} \tag{D4}$$

A. Sub-Functions of f_1

$$f_{1(I_1)} = (r(\kappa_{x_1} + \kappa_{y_1} - r\alpha_1 + r\beta_1)\log(r_i))/2$$

$$f_{1(I_2)} = (r(-(\kappa_{x_2}) - \kappa_{y_2} + r\alpha_2 - r\beta_2)\log(r_i))/2$$

B. Sub-Functions of f_2

$$\begin{aligned}f_{2(I_1)} = &(-3r\epsilon_{x_1})/4 - (3r\epsilon_{y_1})/4 + (r^2\alpha_1)/4 - (x_1^2\gamma_1)/2 \\ &- (r^2\beta_1)/4 - (y_1^2\beta_1)/2 - (r(\epsilon_{x_1} - r\alpha_1)\log(r^{-1}))/2 \\ &- (r(\epsilon_{y_1} + r\beta_1)\log(r^{-1}))/2\end{aligned}$$

$$\begin{aligned}f_{2(I_2)} = &(3r\epsilon_{x_2})/4 + (3r\epsilon_{y_2})/4 - (r^2\alpha_2)/4 + (x_2^2\gamma_2)/2 \\ &+ (r^2\beta_2)/4 + (y_2^2\beta_2)/2 + (r(\epsilon_{x_2} - r\alpha_2)\log(r^{-1}))/2 \\ &+ (r(\epsilon_{y_2} + r\beta_2)\log(r^{-1}))/2\end{aligned}$$

APPENDIX E: COEFFICIENT CALCULATION IN CASE 3

Here are the formulas to calculate the coefficients $\mathcal{M}$ for actuators that can be categorized in *Case 3*:

$r_i \le r_{1e}$,

$$\begin{aligned}\mathcal{M} = (1/(2\pi))&((f_{2(I_{11})}(r_1) - f_{2(I_{11})}(r_{1e})) - f_{2n(I_{11})}\\ &+ (f_{2(I_{12})}(r_1) - f_{2(I_{12})}(r_{1e})) - f_{2n(I_{12})}\\ &+ (f_{2(I_2)}(r_{4e}) - f_{2(I_2)}(r_1)) - f_{2n(I_2)}\\ &+ (f_{2(I_{31})}(r_4) - f_{2(I_{31})}(r_{4e})) - f_{2n(I_{31})}\\ &+ (f_{2(I_{32})}(r_4) - f_{2(I_{32})}(r_{4e})) - f_{2n(I_{32})})\end{aligned} \tag{E1}$$

$r_{1e} < r_i \le r_1$,

$$\begin{aligned}\mathcal{M} = (1/(2\pi))&((f_{1(I_{11})}(r_i) - f_{1(I_{11})}(r_{1e})) - f_{1n(I_{11})}\\ &+ (f_{1(I_{12})}(r_i) - f_{1(I_{12})}(r_{1e})) - f_{1n(I_{12})}\\ &+ (f_{2(I_{11})}(r_1) - f_{2(I_{11})}(r_i)) - f_{2n(I_{11})}\\ &+ (f_{2(I_{12})}(r_1) - f_{2(I_{12})}(r_i)) - f_{2n(I_{12})}\\ &+ (f_{2(I_2)}(r_{4e}) - f_{2(I_2)}(r_1)) - f_{2n(I_2)}\\ &+ (f_{2(I_{31})}(r_4) - f_{2(I_{31})}(r_{4e})) - f_{2n(I_{31})}\\ &+ (f_{2(I_{32})}(r_4) - f_{2(I_{32})}(r_{4e})) - f_{2n(I_{32})})\end{aligned} \tag{E2}$$

$r_1 < r_i \le r_{4e}$,

$$\begin{aligned}\mathcal{M} = (1/(2\pi))&((f_{1(I_2)}(r_i) - f_{1(I_2)}(r_1)) - f_{1n(I_2)}\\ &+ (f_{2(I_2)}(r_{4e}) - f_{2(I_2)}(r_i)) - f_{2n(I_2)}\\ &+ (f_{1(I_{11})}(r_1) - f_{1(I_{11})}(r_{1e})) - f_{1n(I_{11})}\\ &+ (f_{1(I_{12})}(r_1) - f_{1(I_{12})}(r_{1e})) - f_{1n(I_{12})}\\ &+ (f_{2(I_{31})}(r_4) - f_{2(I_{31})}(r_{4e})) - f_{2n(I_{31})}\\ &+ (f_{2(I_{32})}(r_4) - f_{2(I_{32})}(r_{4e})) - f_{2n(I_{32})})\end{aligned} \tag{E3}$$

$r_{4e} < r_i < r_4$,

$$\begin{aligned}\mathcal{M} = (1/(2\pi))&((f_{1(I_{31})}(r_i) - f_{1(I_{31})}(r_{4e})) - f_{1n(I_{31})}\\ &+ (f_{1(I_{32})}(r_i) - f_{1(I_{32})}(r_{4e})) - f_{1n(I_{32})}\\ &+ (f_{2(I_{31})}(r_4) - f_{2(I_{31})}(r_i)) - f_{2n(I_{31})}\\ &+ (f_{2(I_{32})}(r_4) - f_{2(I_{32})}(r_i)) - f_{2n(I_{32})}\\ &+ (f_{1(I_{11})}(r_1) - f_{1(I_{11})}(r_{1e})) - f_{1n(I_{11})}\\ &+ (f_{1(I_{12})}(r_1) - f_{1(I_{12})}(r_{1e})) - f_{1n(I_{12})}\\ &+ (f_{1(I_2)}(r_{4e}) - f_{1(I_2)}(r_1)) - f_{1n(I_2)})\end{aligned} \tag{E4}$$

$r_i \ge r_4$,

$$\begin{aligned}\mathcal{M} = (1/(2\pi))&((f_{1(I_{11})}(r_1) - f_{1(I_{11})}(r_{1e})) - f_{1n(I_{11})}\\ &+ (f_{1(I_{12})}(r_1) - f_{1(I_{12})}(r_{1e})) - f_{1n(I_{12})}\\ &+ (f_{1(I_2)}(r_{4e}) - f_{1(I_2)}(r_1)) - f_{1n(I_2)}\\ &+ (f_{1(I_{31})}(r_4) - f_{1(I_{31})}(r_{4e})) - f_{1n(I_{31})}\\ &+ (f_{1(I_{32})}(r_4) - f_{1(I_{32})}(r_{4e})) - f_{1n(I_{32})})\end{aligned} \tag{E5}$$

A. Sub-Functions of f_1

$$f_{1(I_{11})} = -((-(r\kappa_{x_1}) + r^2\alpha_1)\log(r_i))/2$$

$$f_{1(I_{12})} = -((-(r\kappa_{x_1}) + r^2\alpha_1)\log(r_i))/2$$

$$f_{1(I_2)} = (r(\kappa_{y_1} - \kappa_{y_2} + r\beta_1 - r\beta_2)\log(r_i))/2$$

$$f_{1(I_{31})} = (r(-(\kappa_{x_2}) - \kappa_{y_2} + r\alpha_2 - r\beta_2)\log(r_i))/2$$

$$f_{1(I_{32})} = (r(\kappa_{x_2} + \kappa_{y_1} - r\alpha_2 + r\beta_1)\log(r_i))/2$$

B. Sub-Functions of f_2

$$\begin{aligned}f_{2(I_{11})} = (&-2x_1^2\gamma_1 + r^2\alpha_1(1 + 2\log(r^{-1}))\\ &- r\kappa_{x_1}(3 + 2\log(r^{-1})))/4\end{aligned}$$

$$\begin{aligned}f_{2(I_{12})} = (&-2x_1^2\gamma_1 + r^2\alpha_1(1 + 2\log(r^{-1}))\\ &- r\kappa_{x_1}(3 + 2\log(r^{-1})))/4\end{aligned}$$

$$\begin{aligned}f_{2(I_2)} = (&-(r(\kappa_{y_1} - \kappa_{y_2})(3 + 2\log(r^{-1}))) - \beta_1(r^2 + 2y_1^2\\ &+ 2r^2\log(r^{-1})) + \beta_2(r^2 + 2y_2^2 + 2r^2\log(r^{-1})))/4\end{aligned}$$

$$\begin{aligned}f_{2(I_{31})} = &(3r\epsilon_{x_2})/4 + (3r\epsilon_{y_2})/4 - (r^2\alpha_2)/4 + (x_2^2\gamma_2)/2\\ &+ (r^2\beta_2)/4 + (y_2^2\beta_2)/2 + (r(\epsilon_{x_2} - r\alpha_2)\log(r^{-1}))/2\\ &+ (r(\epsilon_{y_2} + r\beta_2)\log(r^{-1}))/2\end{aligned}$$

$$\begin{aligned}f_{2(I_{32})} = &(-3r\epsilon_{x_2})/4 - (3r\epsilon_{y_1})/4 + (r^2\alpha_2)/4 - (x_2^2\gamma_2)/2\\ &- (r^2\beta_1)/4 - (y_1^2\beta_1)/2 - (r(\epsilon_{x_2} - r\alpha_2)\log(r^{-1}))/2\\ &- (r(\epsilon_{y_1} + r\beta_1)\log(r^{-1}))/2\end{aligned}$$

APPENDIX F: COEFFICIENT CALCULATION IN CASE 4

Here are the formulas to calculate the coefficients $\mathcal{M}$ for actuators that can be categorized in *Case 4*:

$r_i \le r_1$,

$$\begin{aligned}\mathcal{M} = (1/(2\pi))&(((f_{2(I_1)}(r_3) - f_{2(I_1)}(r_1)) - f_{2n(I_1)})\\ &+ ((f_{2(I_2)}(r_2) - f_{2(I_2)}(r_3)) - f_{2n(I_2)})\\ &+ ((f_{2(I_3)}(r_4) - f_{2(I_3)}(r_2)) - f_{2n(I_3)}))\end{aligned} \tag{F1}$$

$r_1 < r_i \le r_3$,

$$\begin{aligned}\mathcal{M} = (1/(2\pi))&(((f_{1(I_1)}(r_i) - f_{1(I_1)}(r_1)) - f_{1n(I_1)})\\ &+ ((f_{2(I_1)}(r_3) - f_{2(I_1)}(r_i)) - f_{2n(I_1)})\\ &+ ((f_{2(I_2)}(r_2) - f_{2(I_2)}(r_3)) - f_{2n(I_2)})\\ &+ ((f_{2(I_3)}(r_4) - f_{2(I_3)}(r_2)) - f_{2n(I_3)}))\end{aligned} \tag{F2}$$

$$r_3 < r_i \le r_2,$$
$$\begin{aligned}\mathcal{M} = (1/(2\pi))(((&f_{1(I_2)}(r_i) - f_{1(I_2)}(r_3)) - f_{1n(I_2)}) \\ &+ ((f_{2(I_2)}(r_2) - f_{2(I_2)}(r_i)) - f_{2n(I_2)}) \\ &+ ((f_{1(I_1)}(r_3) - f_{1(I_1)}(r_1)) - f_{1n(I_1)}) \\ &+ ((f_{2(I_3)}(r_4) - f_{2(I_3)}(r_2)) - f_{2n(I_3)}))\end{aligned} \tag{F3}$$

$$r_2 < r_i < r_4,$$
$$\begin{aligned}\mathcal{M} = (1/(2\pi))(((&f_{1(I_3)}(r_i) - f_{1(I_3)}(r_2)) - f_{1n(I_3)}) \\ &+ ((f_{2(I_3)}(r_4) - f_{2(I_3)}(r_i)) - f_{2n(I_3)}) \\ &+ ((f_{1(I_1)}(r_3) - f_{1(I_1)}(r_1)) - f_{1n(I_1)}) \\ &+ ((f_{1(I_2)}(r_2) - f_{1(I_2)}(r_3)) - f_{1n(I_2)}))\end{aligned} \tag{F4}$$

$$r_i \ge r_4,$$
$$\begin{aligned}\mathcal{M} = (1/(2\pi))(((&f_{1(I_1)}(r_3) - f_{1(I_1)}(r_1)) - f_{1n(I_1)}) \\ &+ ((f_{1(I_2)}(r_2) - f_{1(I_2)}(r_3)) - f_{1n(I_2)}) \\ &+ ((f_{1(I_3)}(r_4) - f_{1(I_3)}(r_2)) - f_{1n(I_3)})).\end{aligned} \tag{F5}$$

A. Sub-Functions of f_1

$$f_{1(I_1)} = (r(\kappa_{x_1} + \kappa_{y_1} - r\alpha_1 + r\beta_1)\log(r_i))/2$$
$$f_{1(I_2)} = (r(\kappa_{x_1} - \kappa_{x_2} - r\alpha_1 + r\alpha_2)\log(r_i))/2$$
$$f_{1(I_3)} = (r(-(\kappa_{x_2}) - \kappa_{y_2} + r\alpha_2 - r\beta_2)\log(r_i))/2$$

B. Sub-Functions of f_2

$$\begin{aligned}f_{2(I_1)} = (&-3r\epsilon_{x_1})/4 - (3r\epsilon_{y_1})/4 + (r^2\alpha_1)/4 - (x_1^2\gamma_1)/2 \\ &- (r^2\beta_1)/4 - (y_1^2\beta_1)/2 - (r(\epsilon_{x_1} - r\alpha_1)\log(r^{-1}))/2 \\ &- (r(\epsilon_{y_1} + r\beta_1)\log(r^{-1}))/2\end{aligned}$$

$$\begin{aligned}f_{2(I_2)} = (&-3r\epsilon_{x_1})/4 + (3r\epsilon_{x_2})/4 + (r^2\alpha_1)/4 - (r^2\alpha_2)/4 \\ &- (x_1^2\gamma_1)/2 + (x_2^2\gamma_2)/2 - (r(\epsilon_{x_1} - r\alpha_1)\log(r^{-1}))/2 \\ &+ (r(\epsilon_{x_2} - r\alpha_2)\log(r^{-1}))/2\end{aligned}$$

$$\begin{aligned}f_{2(I_3)} = (&3r\epsilon_{x_2})/4 + (3r\epsilon_{y_2})/4 - (r^2\alpha_2)/4 + (x_2^2\gamma_2)/2 \\ &+ (r^2\beta_2)/4 + (y_2^2\beta_2)/2 + (r(\epsilon_{x_2} - r\alpha_2)\log(r^{-1}))/2 \\ &+ (r(\epsilon_{y_2} + r\beta_2)\log(r^{-1}))/2\end{aligned}$$

APPENDIX G: COEFFICIENT CALCULATION IN CASE 5

Here are the formulas for calculating the coefficients $\mathcal{M}$ for actuators that can be categorized in *Case 5*:

$$r_i \le r_1,$$
$$\begin{aligned}\mathcal{M} = (1/(2\pi))(((&f_{2(I_1)}(r_2) - f_{2(I_1)}(r_1)) - f_{2n(I_1)}) \\ &+ ((f_{2(I_2)}(r_3) - f_{2(I_2)}(r_2)) - f_{2n(I_2)}) \\ &+ ((f_{2(I_3)}(r_4) - f_{2(I_3)}(r_3)) - f_{2n(I_3)}))\end{aligned} \tag{G1}$$

$$r_1 < r_i \le r_2,$$
$$\begin{aligned}\mathcal{M} = (1/(2\pi))(((&f_{1(I_1)}(r_i) - f_{1(I_1)}(r_1)) - f_{1n(I_1)}) \\ &+ ((f_{2(I_1)}(r_2) - f_{2(I_1)}(r_i)) - f_{2n(I_1)}) \\ &+ ((f_{2(I_2)}(r_3) - f_{2(I_2)}(r_2)) - f_{2n(I_2)}) \\ &+ ((f_{2(I_3)}(r_4) - f_{2(I_3)}(r_3)) - f_{2n(I_3)}))\end{aligned} \tag{G2}$$

$$r_2 < r_i \le r_3,$$
$$\begin{aligned}\mathcal{M} = (1/(2\pi))(((&f_{1(I_2)}(r_i) - f_{1(I_2)}(r_2)) - f_{1n(I_2)}) \\ &+ ((f_{2(I_2)}(r_3) - f_{2(I_2)}(r_i)) - f_{2n(I_2)}) \\ &+ ((f_{1(I_1)}(r_2) - f_{1(I_1)}(r_1)) - f_{1n(I_1)}) \\ &+ ((f_{2(I_3)}(r_4) - f_{2(I_3)}(r_3)) - f_{2n(I_3)}))\end{aligned} \tag{G3}$$

$$r_3 < r_i < r_4,$$
$$\begin{aligned}\mathcal{M} = (1/(2\pi))(((&f_{1(I_3)}(r_i) - f_{1(I_3)}(r_3)) - f_{1n(I_3)}) \\ &+ ((f_{2(I_3)}(r_4) - f_{2(I_3)}(r_i)) - f_{2n(I_3)}) \\ &+ ((f_{1(I_1)}(r_2) - f_{1(I_1)}(r_1)) - f_{1n(I_1)}) \\ &+ ((f_{1(I_2)}(r_3) - f_{1(I_2)}(r_2)) - f_{1n(I_2)}))\end{aligned} \tag{G4}$$

$$r_i \ge r_4,$$
$$\begin{aligned}\mathcal{M} = (1/(2\pi))(((&f_{1(I_1)}(r_2) - f_{1(I_1)}(r_1)) - f_{1n(I_1)}) \\ &+ ((f_{1(I_2)}(r_3) - f_{1(I_2)}(r_2)) - f_{1n(I_2)}) \\ &+ ((f_{1(I_3)}(r_4) - f_{1(I_3)}(r_3)) - f_{1n(I_3)})).\end{aligned} \tag{G5}$$

A. Sub-Functions of f_1

$$f_{1(I_1)} = (r(\kappa_{x_1} + \kappa_{y_1} - r\alpha_1 + r\beta_1)\log(r_i))/2$$
$$f_{1(I_2)} = (r(\kappa_{y_1} - \kappa_{y_2} + r\beta_1 - r\beta_2)\log(r_i))/2$$
$$f_{1(I_3)} = (r(-(\kappa_{x_2}) - \kappa_{y_2} + r\alpha_2 - r\beta_2)\log(r_i))/2$$

B. Sub-Functions of f_2

$$\begin{aligned}f_{2(I_1)} = (&-3r\epsilon_{x_1})/4 - (3r\epsilon_{y_1})/4 + (r^2\alpha_1)/4 - (x_1^2\gamma_1)/2 \\ &- (r^2\beta_1)/4 - (y_1^2\beta_1)/2 - (r(\epsilon_{x_1} - r\alpha_1)\log(r^{-1}))/2 \\ &- (r(\epsilon_{y_1} + r\beta_1)\log(r^{-1}))/2\end{aligned}$$

$$\begin{aligned}f_{2(I_2)} = (&-(r(\kappa_{y_1} - \kappa_{y_2})(3 + 2\log(r^{-1}))) - \beta_1(r^2 + 2y_1^2 \\ &+ 2r^2\log(r^{-1})) + \beta_2(r^2 + 2y_2^2 + 2r^2\log(r^{-1})))/4\end{aligned}$$

$$f_{2(I_3)} = (3r\epsilon_{x_2})/4 + (3r\epsilon_{y_2})/4 - (r^2\alpha_2)/4 + (x_2^2\gamma_2)/2 + (r^2\beta_2)/4 + (y_2^2\beta_2)/2 + (r(\epsilon_{x_2} - r\alpha_2)\log(r^{-1})/2 + (r(\epsilon_{y_2} + r\beta_2)\log(r^{-1}))/2.$$

Funding. H2020 Marie Skłodowska-Curie Actions (DSSC 754315).

Acknowledgment. The authors thank Dr. M. Acuautla and Prof. B. Noheda of the University of Groningen, and Dr. S. N. R. Kazmi, M. Eggens, and H. Smit of the Netherlands Institute for Space Research for their valuable input on the Hysteretic Deformable Mirror project. In addition, we would like to thank the Center for Information Technology of the University of Groningen for support and for providing access to the Peregrine high-performance computing cluster.

Disclosures. The authors declare no conflicts of interest.

REFERENCES

1. R. J. Zawadzki, S. M. Jones, S. S. Olivier, M. Zhao, B. A. Bower, J. A. Izatt, S. Choi, S. Laut, and J. S. Werner, "Adaptive-optics optical coherence tomography for high-resolution and high-speed 3D retinal in vivo imaging," Opt. Express **13**, 8532–8546 (2005).
2. W. J. Shain, N. A. Vickers, B. B. Goldberg, T. Bifano, and J. Mertz, "Extended depth-of-field microscopy with a high-speed deformable mirror," Opt. Lett. **42**, 995–998 (2017).
3. M. J. Booth, "Adaptive optics in microscopy," Phil. Trans. R. Soc. A. **365**, 2829–2843 (2007).
4. E. J. Fernández, I. Iglesias, and P. Artal, "Closed-loop adaptive optics in the human eye," Opt. Lett. **26**, 746–748 (2001).
5. G. Vdovin and V. Kiyko, "Intracavity control of a 200-W continuous-wave Nd:YAG laser by a micromachined deformable mirror," Opt. Lett. **26**, 798–800 (2001).
6. J. W. Hardy, *Adaptive Optics for Astronomical Telescopes*, Oxford Series in Optical and Imaging Sciences (Oxford University, 1998).
7. T. Sato, H. Ishida, and O. Ikeda, "Adaptive PVDF piezoelectric deformable mirror system," Appl. Opt. **19**, 1430–1434 (1980).
8. K. L. Wlodarczyk, E. Bryce, N. Schwartz, M. Strachan, D. Hutson, R. R. J. Maier, D. Atkinson, S. Beard, T. Baillie, P. Parr-Burman, K. Kirk, and D. P. Hand, "Scalable stacked array piezoelectric deformable mirror for astronomy and laser processing applications," Rev. Sci. Instrum. **85**, 024502 (2014).
9. S. A. Cornelissen, A. L. Hartzell, J. B. Stewart, T. G. Bifano, and P. A. Bierden, "MEMS deformable mirrors for astronomical adaptive optics," Proc. SPIE **7736**, 898–907 (2010).
10. G. Vdovin and M. Loktev, "Deformable mirror with thermal actuators," Opt. Lett. **27**, 677–679 (2002).
11. L. Huang, X. Ma, M. Gong, and Q. Bian, "Experimental investigation of the deformable mirror with bidirectional thermal actuators," Opt. Express **23**, 17520–17530 (2015).
12. R. G. Gilbertson and J. D. Busch, "A survey of micro-actuator technologies for future spacecraft missions," J. Br. Interplanet. Soc. **49**, 129–138 (1996).
13. R. Biasi, D. Gallieni, P. Salinari, A. Riccardi, and P. Mantegazza, "Contactless thin adaptive mirror technology: past, present, and future," Proc. SPIE **7736**, 872–885 (2010).
14. P.-Y. Madec, "Overview of deformable mirror technologies for adaptive optics and astronomy," Proc. SPIE **8447**, 22–39 (2012).
15. The LUVOIR Team, "The LUVOIR mission concept study final report," arXiv: 1912.06219 (2019).
16. R. H. Freeman and J. E. Pearson, "Deformable mirrors for all seasons and reasons," Appl. Opt. **21**, 580–588 (1982).
17. P. Riaud, "New high-density deformable mirrors for high-contrast imaging," Astron. Astrophys. **545**, A25 (2012).
18. R. Huisman, M. Bruijn, S. Damerio, M. Eggens, S. N. R. Kazmi, A. E. M. Schmerbauch, H. Smit, M. A. Vasquez Beltran, E. van der Veer, M. Acuautla, B. Jayawardhana, and B. Noheda, "High pixel number deformable mirror concept utilizing piezoelectric hysteresis for stable shape configurations," arXiv: 2008.09338.
19. M. A. Vasquez-Beltran, B. Jayawardhana, and R. Peletier, "Recursive algorithm for the control of output remnant of Preisach hysteresis operator," IEEE Control Systems Letters, **5**, 1061–1066 (2021).
20. E. S. Claflin and N. Bareket, "Configuring an electrostatic membrane mirror by least-squares fitting with analytically derived influence functions," J. Opt. Soc. Am. A **3**, 1833–1839 (1986).
21. V. Lakshminarayanan and A. Fleck, "Zernike polynomials: a guide," J. Mod. Opt. **58**, 1678 (2011).
22. L. Huang, C. Rao, and W. Jiang, "Modified Gaussian influence function of deformable mirror actuators," Opt. Express **16**, 108–114 (2008).
23. R. K. Tyson, *Adaptive Optics Engineering Handbook* (CRC Press, 1999).
24. R. K. Tyson and B. W. Frazier, *Field Guide to Adaptive Optics* (SPIE, 2004).
25. R. F. M. M. Hamelinck, *Adaptive Deformable Mirror: Based on Electromagnetic Actuators* (Technische Universiteit Eindhoven, 2010).
26. R. P. Grosso and M. Yellin, "The membrane mirror as an adaptive optical element," J. Opt. Soc. Am. **67**, 399–406 (1977).
27. L. Arnold, "Optimized axial support topologies for thin telescope mirrors," Opt. Eng. **34**, 567–574 (1995).
28. S. K. Ravensbergen, R. F. M. M. Hamelinck, P. C. J. N. Rosielle, and M. Steinbuch, "Deformable mirrors: design fundamentals for force actuation of continuous facesheets," Proc. SPIE **7466**, 74660G (2009).
29. L. Arnold, "Uniform-load and actuator influence functions of a thin or thick annular mirror: application to active mirror support optimization," Appl. Opt. **35**, 1095–1106 (1996).
30. L. Arnold, "Influence functions of a thin shallow meniscus-shaped mirror," Appl. Opt. **36**, 2019–2028 (1997).
31. K. Bush, D. German, B. Klemme, A. Marrs, and M. Schoen, "Electrostatic membrane deformable mirror wavefront control systems: design and analysis," Proc. SPIE **5553**, 28–38 (2004).
32. A. Menikoff, "Actuator influence functions of active mirrors," Appl. Opt. **30**, 833838 (1991).
33. T. Ruppel, "Modeling and control of deformable membrane mirrors," in *Adaptive Optics Progress*, (IntechOpen, 2012), pp. 99–123.
34. P. M. Morse and H. Feshbach, *Methods of Theoretical Physics, Part II* (McGraw-Hill, 1953).
35. B. Jayawardhana, M. A. Vasquez-Beltran, W. J. van de Beek, C. de Jonge, M. Acuautla, S. Damerio, R. Peletier, B. Noheda, and R. Huisman, "Modeling and analysis of butterfly loops via Preisach operators and its application in a piezoelectric material," in *IEEE Conference on Decision and Control (CDC)* (2018), pp. 6894–6899.
36. M. A. Vasquez-Beltran, B. Jayawardhana, and R. Peletier, "Asymptotic stability analysis of Lur'e systems with butterfly hysteresis nonlinearities," IEEE Control Syst. Lett. **4**, 349–354 (2020).